Design of a static test rig for advanced seals and air bearing testing

Anna Zimmermann, Rogier Giepman, Tue Nguyen Tran, Christian Aalburg, Volker Gümmer

Design of a static test rig for advanced seals and air bearing testing

A.-L. Zimmermann[1]*, R. H. M. Giepman[2], Q. T. Nguyen Tran[2], C. Aalburg[2], V. Gümmer[1]

ISROMAC 2017

International Symposium on Transport Phenomena and Dynamics of Rotating Machinery

Maui, Hawaii

December 16-21, 2017

Abstract

Today's industrial gas turbines are required to cope with strong fluctuations caused by a strongly varying feed of renewable energies into the grid. These transient operating conditions result in high temperature gradients and consequently lead to increased axial and radial displacements of turbine parts. Such flexible operations need to be supported by novel sealing technologies. This paper presents a new test facility for investigating advanced seals under 2D static conditions. It facilitates detailed experimental studies of the static pressure distribution on the seal air bearing faces, measurements on the leakage flow through the seal and measurements on the air bearing force balance. The clearance between the rotor and the seal can be set very accurately and it is furthermore possible to apply a predetermined amount of eccentricity to the seal / rotor combination.

Keywords

advanced seals — aerodynamic characterization — air bearing — pressure distribution on the bearing surface — static test rig

[1] *Technical University of Munich, Germany, Department of Mechanical Engineering, Institute of Turbomachinery and Flight Propulsion*

[2] *GE Global Research, Garching, Germany*

*__Corresponding author__: anna.zimmermann@ltf.mw.tum.de

INTRODUCTION

The increasing share of renewables on the electrical grid makes the supply side of the grid less predictable than it used to be. Large fluctuations may occur, which are to be compensated by the traditional sources of electricity, like gas turbines [1]. Today's gas turbines are, however, designed for high performance operation in a base-load regime and their design is not well focused on quickly changing load requirements. Flexible operation cycles result in high temperature gradients coupled with large axial and radial displacements of turbine parts and are currently limited by the tight clearance between the rotor and stator. Novel technologies thus need to be introduced to balance demand peaks by providing flexible operation, while still increasing the performance of gas turbines. Current sealing concepts are particularly affected, so that advanced seal design concepts need to be invented, optimized and tested at engine-representative conditions to match the latest requirements on turbomachinery.

Adaptive seals present a promising approach to allow transient operations and reduced leakage flows. They ensure minimal clearances and can handle a wide range of operating conditions [2]. The seal is spring-mounted allowing it to follow the rotor's axial movements and small feed holes are present on the seal's surface. These feed holes inject high-pressure air in the rotor / stator gap, effectively creating a hydrostatic gas bearing between both components. Performance of these gas bearings and consequently the design and optimization have been the subject of various studies. Of special interest here are: the stiffness, damping, load carrying capacity, flow rate and stability of the air bearing [3].

As a necessary first phase in designing an adaptive seal the static characteristics of air bearings are to be understood [4]. This determines the general feasibility. Subsequently, a rotating test rig is developed [1], which is outside the scope of this paper, to address the dynamic behaviors of the seal. Nishio et al. [5] investigated both static and dynamic characteristics of air bearings with feed holes of less than 0.05 mm in diameter and focused on the effect of the surface roughness on the bearing characteristics. Fourka et al. [6] developed a numerical approach to predict the stability of air bearings, which was supported by some experimental test results. A similar research approach with a similar test facility was developed by Franssen et al. [7]. All test facilities mentioned allow the investigation of the load capacity, but there has been no study covering the exact pressure distribution on the air bearing surface. Such measurements are, however, of great interest since the pressure in the end translates back to the air bearing's stiffness, which guarantees a non-contact operation of the seal. Also, for the sake of validating and improving the numerical codes [8–11] used for simulating the behavior of adaptive seals it would be helpful to have accurate pressure distributions available.

In this paper a new test facility is presented which allows to study advanced seals within a static test environment. The static characterization is of fundamental interest to assure a successful application of the seal. The gained findings can provide a deeper understanding of the air bearing behavior and can be fed into dynamic tests as a next step towards

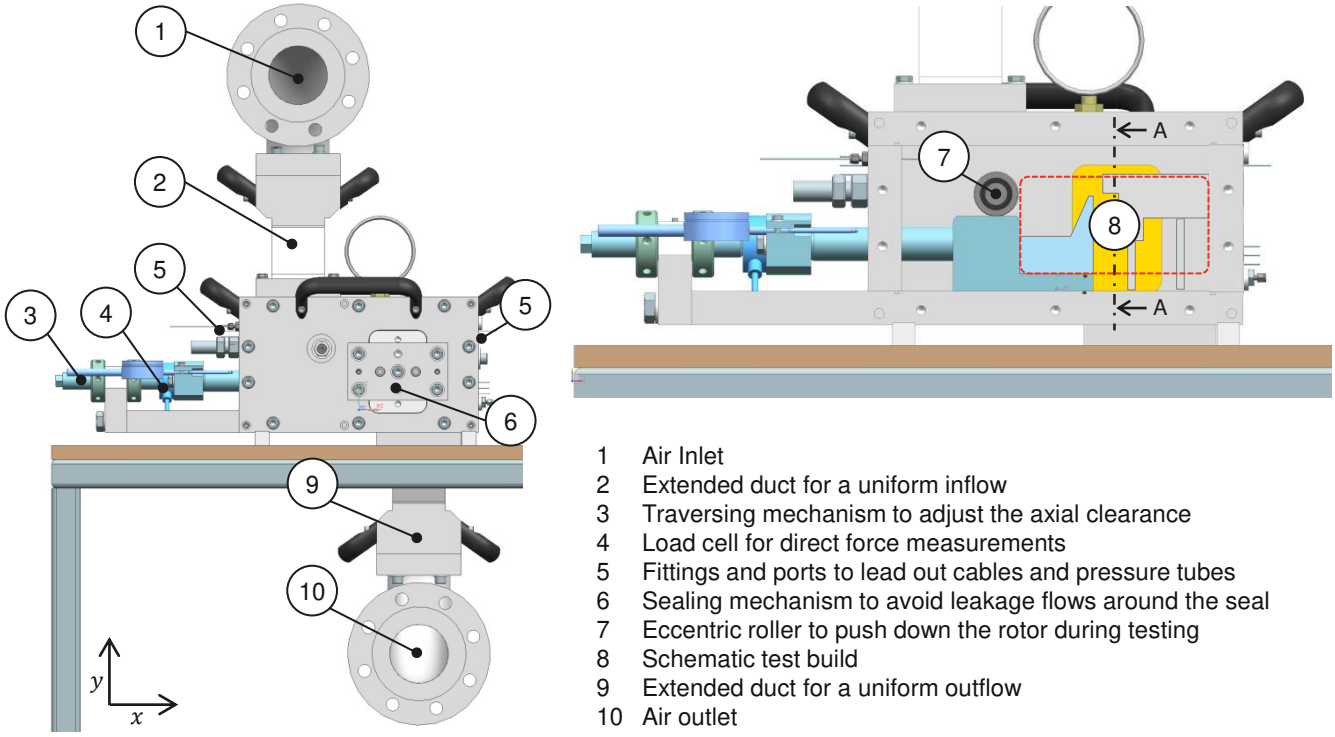

1 Air Inlet
2 Extended duct for a uniform inflow
3 Traversing mechanism to adjust the axial clearance
4 Load cell for direct force measurements
5 Fittings and ports to lead out cables and pressure tubes
6 Sealing mechanism to avoid leakage flows around the seal
7 Eccentric roller to push down the rotor during testing
8 Schematic test build
9 Extended duct for a uniform outflow
10 Air outlet

Figure 1. Design overview

engine relevant testing conditions. However, the present test facility enables in-depth studies of the aerodynamic properties of advanced seals with a major focus on the air bearing flow. Both the design and measurement concept of the rig are described and a comprehensive study of the measurement uncertainties is presented.

1. TEST RIG

1.1 Rig capabilities

The new test facility was developed to test advanced seal designs under various Reynolds and Mach numbers, representing realistic gas turbine conditions. A 2D straight segment of such an advanced seal or air bearing can be fitted into the rig while its modular design supports a quick exchange of the interchangeable test build. Consequently, various types of test builds can be tested without great effort and within short periods of time. The rig allows for the horizontal and vertical gap adjustment to simulate different axial and radial clearances, respectively. It is also possible to set a certain eccentricity of the air bearing in the radial direction. Numerical studies of an optimized inlet and outlet design were done to ensure uniform flow conditions across the span of the seal.

The leakage across the seal is one of the key outcomes of the planned measurement campaigns. Special effort was therefore placed on sealing all parasitic leakage paths, in particular: 1) leakage out of the housing and 2) leakage around the test build, instead of through the test build. Additionally, the rig is capable of force measurements to quantify the load acting on the bearing face. Selected measures were planned into the test rig concept to minimize system-inherent friction forces during the force measurement. A summary of the main rig capabilities is given in Tab. 1.

Table 1. Rig capabilities

Maximum pressure:	10 bar
Maximum mass flow rate:	0.75 kg/s
Horizontal traverse:	up to 58 mm
Vertical adjustment:	at least ±0.38 mm
Measurements:	Mass flow, clearance, static pressure, force

1.2 Design overview

Fig. 1 shows the design overview of the new test facility. Pressurized air enters the rig through the air inlet and is guided to the inside of the rig. The extended geometry of the inlet duct hereby ensures a uniform inlet flow across the entire span of the seal. After the air flow passes the test build it exits the rig through the extended duct and outlet, whereby the test build could either be a seal or a bearing.

The test build is interchangeable and always consists of two units: A 2D rotor and a seal model. Fig. 2a) represents a sectional view of an exemplary test build. As it is schematically shown, the seal possesses two different types of flow ducts: Equally distributed feed holes serve as supply ducts to establish the air film at the bearing face, whereby multiple air ducts, which are also equally distributed over the span of the model, are in place to ensure a low static pressure in

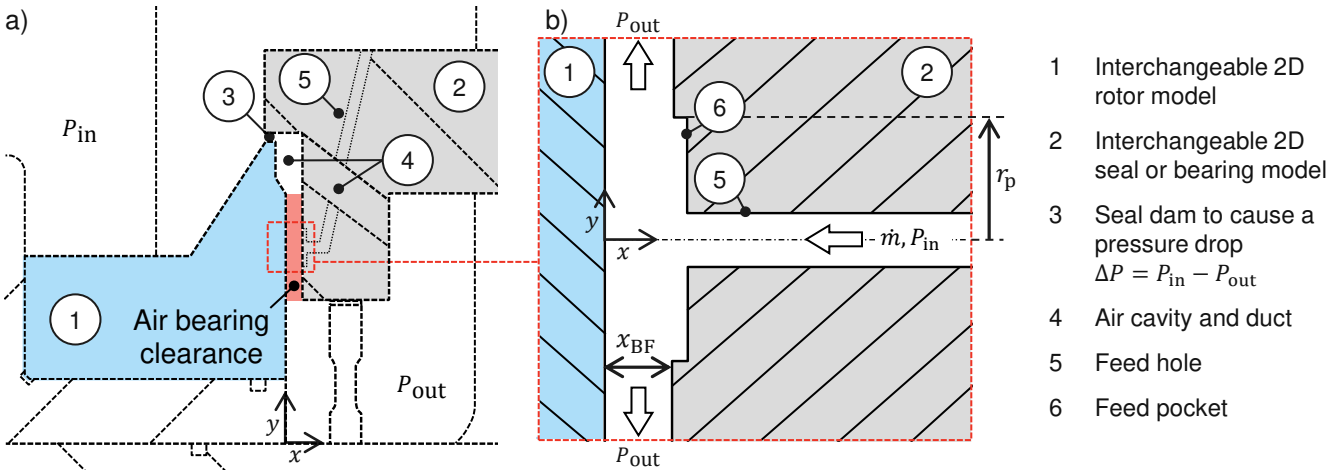

Figure 2. Schematic view of a) the test build design and b) the air bearing design

the air cavity above the bearing face. A shallow pocket with radius r_p is embedded around the feed hole exit. Since the most interesting area to be examined is the bearing face, it is schematically illustrated in Fig. 2b). The air flow comes from the high pressure area P_{in} upstream the seal and is fed through the feed hole into the bearing clearance with the axial gap width x_{BF}. The flow impinges on the opposite bearing surface of the rotor and escapes continuously to the low pressure area P_{out} downstream the seal.

The rotor and the seal are equipped with a total of 66 pressure taps to allow for an accurate reconstruction of the flow field afterwards. Metal tubes with an outer diameter of 1.1 mm or 1.6 mm are on the models and the rig's sidewalls and are connected through plastic pressure tubing. These are then hooked up to the pressure scanners outside the rig. Furthermore, the rotor features 3 flush-mounted proximity probes, which are used for tracking the seal / rotor clearance across its full-span.

1.2.1 Gap adjustment

Axial gap. The traversing mechanism illustrated in Fig. 3 is used to set the axial gap width at the bearing face between seal and rotor. The rotor model can be mounted on the slider, which is axially guided by two rods. A stepless adjustment of the axial gap width can be realized by using the screw mechanism comprising two counterrotating nuts screws engaged on the threaded rod. The distance between rotor and seal is measured by 3 proximity probes, which have an axial range up to 2 mm, and the two dial gauges outside the rig. The gauges also help to detect and remove any model tilt. To ensure a fixed position of the rotor during testing, multiple features are present and can be applied: First, by tightening the two counterrotating nuts against each other, the rotor movement can be blocked. Second, two eccentric rollers on both rig sidewalls can be used to additionally push the rotor / slider unit against the bottom plate. Third, a pair of limit stops can be clamped between rotor and the rig's backwall to facilitate the gap adjustment and to block any kind of rotor movement during rig operation.

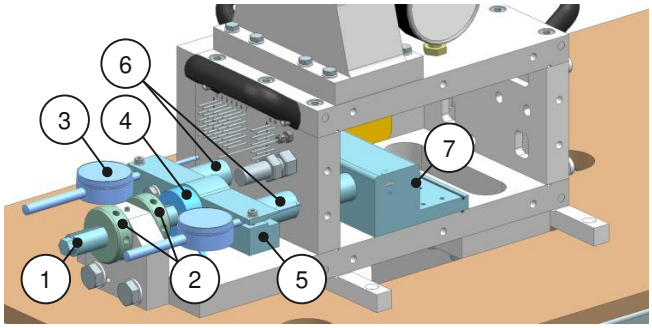

Figure 3. Axial traversing mechanism

Radial gap. The seal model is attached firmly to the backwall of the rig and is furthermore supported by 3 vertical rods to minimize any deformation during rig operation (see Fig. 4). The length of the rods can be varied stepwise by adding shims of different thicknesses. This setup allows for a variation of ±0.38 mm in the radial gap size. Additionally, a thin shim can be inserted between the rotor and slider to have the rotor and seal surface tilted with respect to each other.

1.2.2 Sealing features

The test rig has been designed to provide accurate mass flow measurements of the leakage flow across the seal / rotor combination. Therefore, it is important to remove or properly seal all parasitic leakage flow paths: 1) air leaking out of the housing, 2) air leaking around the seal / rotor housing.

Well-placed sealing rings are used to block the air flow out of the housing and an ingenious sealing mechanism at both sidewalls, see Fig. 5, minimizes the air leaking between the test build and the housing walls. Eventually, two rubber shims added to a pressure fitting can be pushed against the test build to consequently seal all critical areas. The pressure fitting is hereby linearly guided by a guiding rod and the two

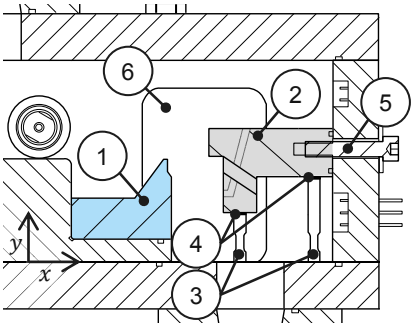

Figure 4. Mechanisms to adjust the radial gap width

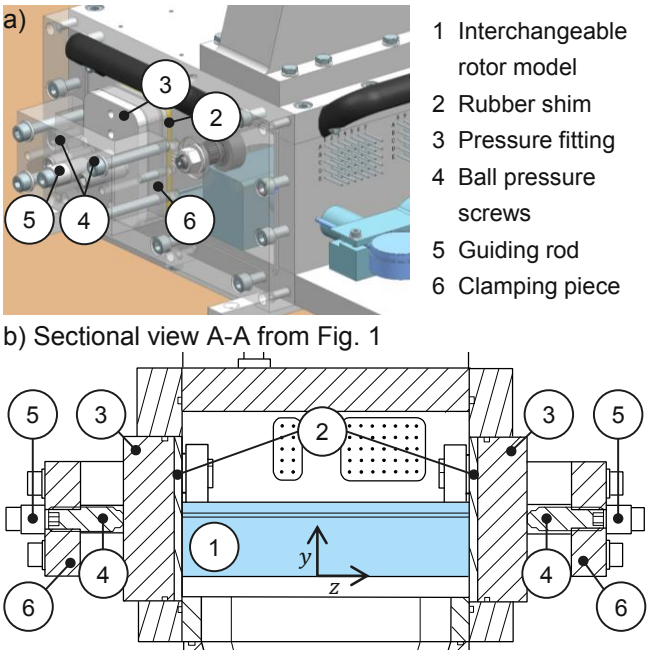

Figure 5. Sidewall sealing mechanism

ball pressure screws are used to apply the required pressure force. A potential leakage flow at the seal's back is considered and mostly avoided by adding a sealing ring to its assembly. Applying a sealing fluid on all contact areas, additionally, minimizes remaining leakage flows.

1.2.3 Rigid design

A structural analysis of all components was made to ensure a stiff design to minimize the deformation of the bearing surfaces while testing. The expected deformations at the bearing surfaces in axial direction were calculated to be less than 2.5 μm at maximum operation pressures. These deformations are substantially smaller than the machining tolerances of 13 μm and can be neglected.

2. MEASUREMENT SYSTEM

A comprehensive measurement system to measure mass flow rate, static pressure, clearance and force was built up and allows for a detailed characterization of the air bearing flow.

The data acquisition is accomplished by a NI CompactDAQ, which is equipped with multiple input and output NI modules. All modules have a 16-bit resolution and 200 kS/s aggregate sampling rate.

2.1 Mass flow

The test rig is connected to the local GE screw compressor, which delivers up to 0.75 kg/s pressurized air with maximum 10 bar absolute pressure. The mass flow measurement is done by one of two parallel Coriolis flow meters of type Promass 80F by Endress+Hauser, both installed upstream of the rig, and each flow meter is adjusted for a different mass flow range. While the first meter is for mass flow rates up to 0.1 kg/s, the second covers mass flow rates between 0.1 kg/s and 0.75 kg/s. The inlet mass flow rate can be either mass flow or pressure controlled. Downstream of the rig a control valve is installed to also control the outlet mass flow. By a controlled closing of the valve the backpressure required downstream of the seal can be set accurately.

Uncertainty of mass flow measurements. The measured error of the flow meter device is indicated with ±0.5 % of full scale. Furthermore, the mass flow measurements are affected by, first, unwanted leakage paths around the seal / rotor combination inside of the test rig and, second, by leakage from the inside to the outside of the test rig. Multiple leak tests were performed to quantify the remaining leakage rate of the rig. During all tests either the rig's outlet or the seal was fully closed and via the inlet the rig was pressurized up to a certain pressure level. The rate of depressurization could subsequently be used to infer the leakage flow: The leakage inside the rig around the seal / rotor combination is calculated to be less than 0.2 %, and less than 0.02 % from the inside to the outside of the rig. Tab. 2 sums up all proportions of uncertainty of the mass flow measurement.

Table 2. Uncertainty of mass flow measurements

Source	Uncertainty [%]
Flow meter accuracy	±0.5
In-rig leakage (around seal / rotor)	0.2
In-to-out rig leakage	0.02
Overall uncertainty	−0.5 … 0.72

Repeatability of mass flow measurements. A number of operation conditions were repeated multiple times and evaluated with regard to the mass flow repeatability. At mass flow rates of ~ 0.045 kg/s the repeatability error is ±1.6 %. This value decreases for mass flow rates smaller than 0.045 kg/s.

2.2 Static pressure

Before starting the experimental tests, a pre-study based on CFD simulations was done to estimate the distribution of static pressures at the rotor's bearing surface. Fig. 6a) shows the CFD result at a chosen segment of the rotor's bearing face

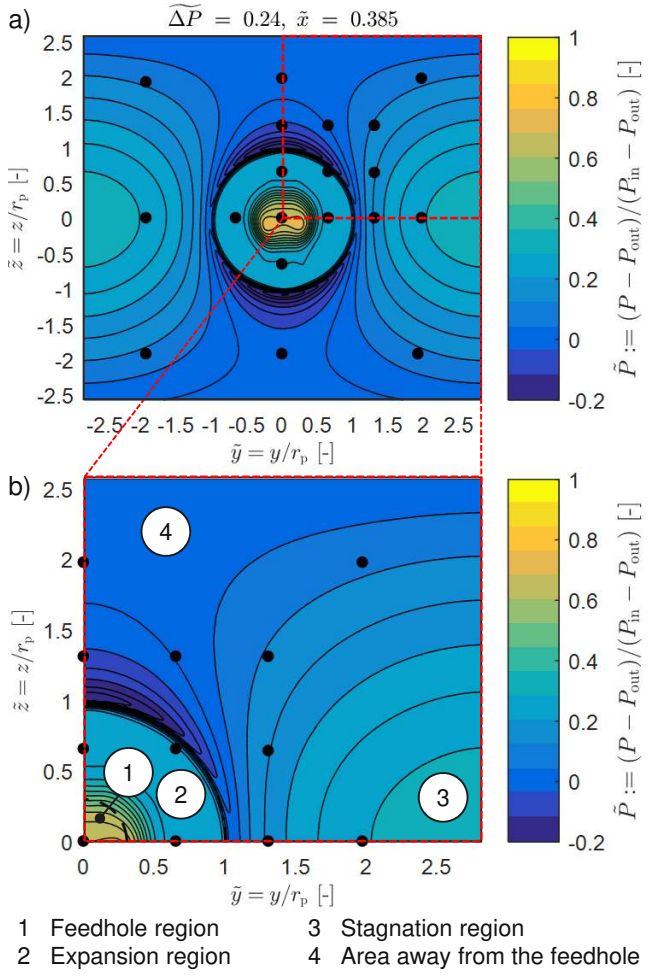

Figure 6. Expected pressure distribution on the bearing surface of the rotor for representative operating conditions gained from CFD simulations

at representative differential pressure $\widetilde{\Delta P} := (P_{in} - P_{out})/P_{in}$ and axial clearance $\tilde{x} := x_{BF}/r_p$, whereas r_p is the radius of the feed pocket. The segment is located opposite of the feed hole and captures the full height of the bearing face (z-direction) and a small portion in the horizontal direction (y-direction). The feed hole flow impinges at the center of the segment, more specifically the origin of the coordinate system and from there on spreads out into both y- and z-directions.

Due to a symmetrical spread of the flow it is sufficient to only investigate the flow within one quarter of the segment in detail, see Fig. 6b).

The bearing face flow can basically be divided into two flow regimes: A radial flow expands in z-direction from the high pressure ($\sim P_{in}$) at the feed hole region to the low pressure ($\sim P_{out}$) at the upper or bottom edge of the bearing face; due to the presence of an adjacent feed hole outside the segment, a circumferential flow expands from the high pressure at the feed hole to a stagnation pressure in between the feed holes. Consequently, the flow in the latter regime first follows the y-direction but is then deflected into the z-direction and eventually merges with the flow in the radial regime.

Table 3. Uncertainty of static pressure measurements

Source	Uncertainty [%]
DSA accuracy	±0.05
Flatness tolerance	
– Away from feed hole	±1.5
– At expansion region	±6
– At feed hole region	±3
Diameter of pressure taps	
– Away from feed hole	±0.01
– At expansion region	±5
– At feed hole region	±0.2
Positioning of pressure taps	
– Away from feed hole	±0.1
– At expansion region	±10
– At feed hole region	±1
Overall uncertainty	
– Away from feed hole	±1.66
– At expansion region	±21.05
– At feed hole region	±4.25

The CFD results were used to optimize the distribution of the pressure taps across the bearing surface such that all important flow features can be captured: the feed hole, expansion and stagnation region as well as the area away from the feed hole. Since the numerical result predicted 4 nearly identical quarters around the feed hole, the authors decided to investigate only one quarter of the segment in detail. The black markers in Fig. 6a) and b) illustrate the final pressure tap pattern on the rotor's bearing surface. As it can be seen, the first quarter possesses the largest amount of pressure taps, while some additional taps are located in the other quarters to confirm the symmetry assumption. More pressure taps were also fitted on the seal to measure pressures upstream and downstream of the bearing face and to check for flow uniformity.

The pressure measurements were performed with multiple Scanivalve pressure scanners of type DSA3218 in different operating ranges.

Uncertainty of pressure measurements. First, the vendor given accuracy of the pressure scanner modules must be captured. The accuracy here is stated with ±0.05 % of the full scale. Second, the pressure measurements are affected by the flatness tolerances ($\sim$ 13 μm) that can be obtained for the tested seal / rotor combination, the diameter of the taps ($\sim$ 0.3 mm) and their positioning accuracy ($\sim$ 0.05 mm), respectively. To assess the different impacts, CFD calculations were performed for the desired experimental conditions. The results are illustrated in Fig. 7a)-c). As it can be seen, very accurate pressure measurements are possible away from the feed hole and the expansion region, but they are difficult in its near vicinity. Hence, it is preferable to define 3 uncertainty ranges: Pressure measurements close to the expansion region

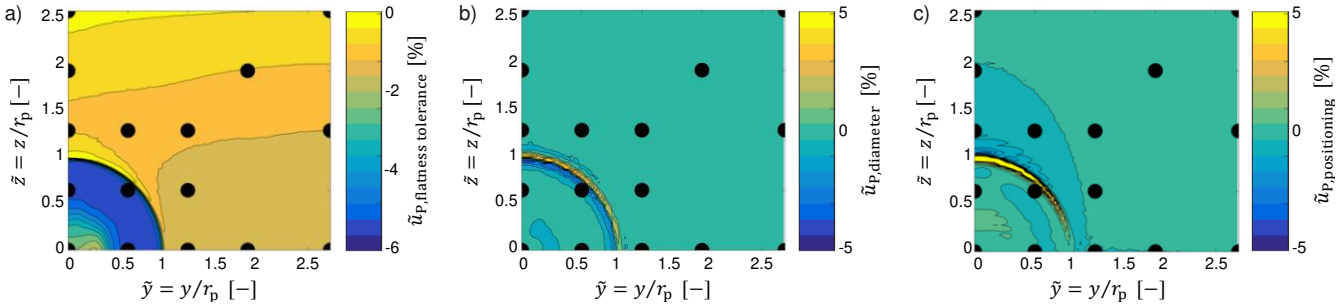

Figure 7. Uncertainty on the pressure measurements caused by a) the flatness tolerance on the bearing surface, b) the diameter of the pressure taps and c) the positioning accuracy of the pressure taps

are possible with a maximum uncertainty of ±21.05 %, while pressure measurements close to the feed hole are possible with an intermediate uncertainty of ±4.25 %. All pressure measurements away from these regions are less critical and an uncertainty of ±1.66 % is considered. A summary of the different contributions is given in Tab. 3.

Repeatabilty of pressure measurements. The experiments were repeated multiple times on different days. Subsequently, the measurement data could be analyzed with a special focus on its repeatability. By so doing, 3 different ranges were defined again: The repeatability error is highest near the expansion region (±0.7 %), intermediate near the feed hole region (±0.3 %) and smallest away from the feed hole and expansion region (±0.2 %).

2.3 Clearance

The axial gap x_{BF} between the seal's and rotor's bearing face is measured by 3 Capacitec's HPT-150 non-contact probes, which are distributed along the bearing face span of the rotor. In doing so, a uniform gap width over the entire bearing face width can be ensured and quantified. The capacitive sensors were delivered including a calibration record wherein an accuracy of ±0.5 μm was specified. To achieve and maintain high accuracy, the probes are calibrated in regular intervals. The calibration is executed separately for every probe and in accordance with the following protocol:

Calibration protocol. Figure 8 shows the calibration unit, which was designed to calibrate the proximity probes embedded into the rotor model. The unit consists of 3 main modules: a robust holding block ensures a safe stand on the model surface; a distance rod with integrated limit stop allows for the precise positioning of the calibration bolt above the proximity probe; a micrometer screw gauge measures the adjusted clearance between proximity probe and calibration bolt. First, the unit is positioned right next to one proximity probe and the micrometer screw gauge is zeroed. Using this zero value the holder can be subsequently placed above the probe to start the calibration. While moving up the calibration bolt stepwise, the corresponding voltage is acquired. The calibration procedure is thereafter repeated for all proximity probes, whereby the zero setting is not changed in between the probes. In general, the calibration result confirms, that

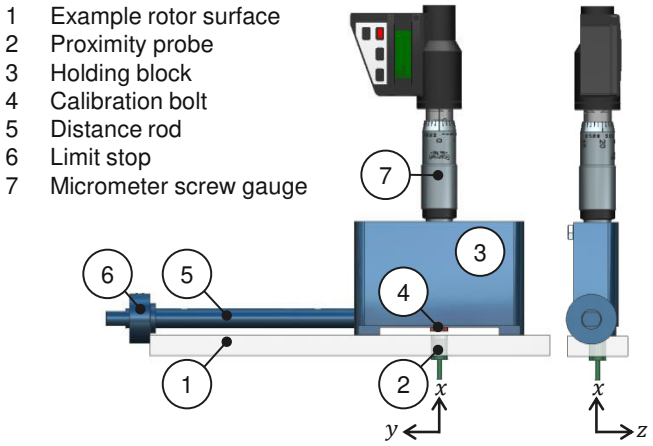

Figure 8. Calibration unit

the sensor signal is approximately linear within the range of $x = 0 \ldots 0.6 \cdot x_{max}$, where $x_{max} = 2$ mm is the maximum sensor range.

Uncertainty of clearance measurements. Evaluating the total uncertainty of the clearance measurement, multiple contributions need to be considered. While the sensor itself has a systematic error of ±0.5 μm, the error due to the calibration needs to be looked at as well. The calibration error comes from 2 different sources: First, a constant shift of the input-output calibration curve is expected as a result of zeroing the micrometer screw gauge. Repeated zero calibrations by several users show that the wall location can be determined with an accuracy of ±13 μm. Second, interpolating the calibration measurement points to a linear calibration curve adds a systematic error of maximum ±2.5 μm. While the listed uncertainties are caused by the calibration of the probes, an additional contribution comes from the test setup itself and has to be added to the total uncertainty of the clearance measurement. This uncertainty is found in a possible tilt of the rotor inside the rig while testing. Such a tilt can cause a non-uniform gap over the model span and needs to be quantified. On average the occurring tilt error is in the range of ±5 μm. Summing up all contributions, see Tab. 4, a mean uncertainty on the clearance measurement of about ±21 μm is recorded.

Table 4. Uncertainty of clearance measurements

Source	Uncertainty [μm]
Proximity probe accuracy	±0.5
Zero adjustment	±13
Calibration interpolation	±2.5
Tilt of the rotor	±5
Overall uncertainty	±21

Table 5. Uncertainty of force measurements

Source	Uncertainty [%]
Estimation of friction force	±(7 … 16)
Load cell accuracy	±13
Machining precision of A_{BF}	±0.2
Pressure measurement accuracy	±0.5
Overall uncertainty	±(20.7…29.7)

Repeatability of clearance measurements. By evaluating multiple repeated calibrations, the repeatability error of the gap measurements was assessed. It is maximum ±15 μm.

2.4 Force

A load cell of type LCM204 from Omega is installed in the traversing mechanism of the rig (cf. Fig. 3) to measure the force acting on the rotor. Due to large contact surfaces between the rotor assembly and the test rig housing system-inherent friction forces are expected. For this reason, the rig setup has several mechanisms implemented to minimize the effect of friction. Almost all mechanisms, which are originally applied for sealing purposes, can be removed: The two rubber shims of the sidewall sealing mechanism can be replaced by flush mounted metal side plates and all affecting rubber sealing elements can be removed. Additionally, the eccentric rollers can stay in a released position. Even though all these measures come along with an increased leakage around the seal, they are accepted for the single event of force measurement. However, a remaining friction force is still expected, which is why a procedure is introduced to estimate and correct for the effects of friction on the force measurement. Once the friction force is known, it can be used to quantify the force F_{BF} acting on the bearing face, which is a crucial outcome of this study. The force can be derived from the force balance equation

$$F_{BF} = F_{in} - F_{out} - F_{cav} - F_{LC} - F_f, \tag{1}$$

where F_{in} represents the force due to pressure P_{in} acting on the inlet side of the seal and F_{out} represents the force due to the outlet pressure P_{out}. Additionally, in between the rotor and the seal one can distinguish between the force F_{cav} established in the air duct cavity and the force F_{BF} coming from the bearing face. All forces are illustrated in Fig. 9.

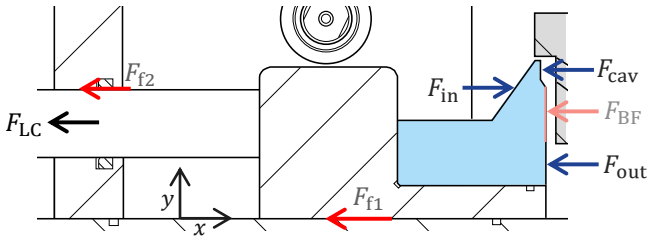

Figure 9. Force balance in axial direction

Calibration of friction force. The friction force can be estimated by opening the seal / rotor combination. The pressure on the left-end of the rotor then equals P_{in}, whereas on the right it equals P_{out}. In a hypothetical no-friction case one would expect to record the following force by the load cell:

$$F_{id} = A \cdot (P_{in} - P_{out}), \tag{2}$$

where A represents the projected area. The difference between the ideal force F_{id} and the recorded force by the load cell F_{LC} can then be used as an estimate for the friction force

$$F_f = F_{id} - F_{LC}. \tag{3}$$

Since the friction force is dependent on the differential pressure across the seal, the calibration needs to be performed for all operating pressure conditions P_{in} and P_{out}. Some effects of hysteresis were encountered when performing this calibration procedure, that is, the friction forces differed slightly between a calibration campaign where the pressures were progressively increased or decreased. To compensate this effect, two separate calibrations curves are defined: One curve to quantify F_f for an ascending pressure mission and another curve to describe F_f a descending pressure mission.

Uncertainty of force measurements. F_{BF} is the most crucial force in this study. It is gained from Eq. 1 and depends on various quantities and their uncertainties. A first and major uncertainty hereby comes from the estimation on the effect of friction forces. The estimation is based on a semi-empirical approach and we consequential assume an uncertainty of ±(7 … 16) % at a conservative evaluation. Second, the uncertainty caused by the load cell itself has to be considered. According to the load cell's specification the different sources (linearity, hysteresis and repeatability) contribute to a total uncertainty of ±0.3 % of the full scale output. This affects the result of F_{BF} by maximum ±13 %. Since F_{BF} is a calculated and not directly measured quantity, both the uncertainty coming from the pressure measurements and the uncertainty resulting from the manufacturing must be looked at as well. The pressure measurements are very accurate so that their impact on the force result is only small with ±0.2 %. Furthermore, for each linear dimension a maximum tolerance of ±13 μm due to machining precision is known. This affects the result of F_{BF} by less than ±0.5 %. Summing up all shares, see Tab. 5, the overall uncertainty of F_{BF} is in the range of ±(20.7…29.7) %.

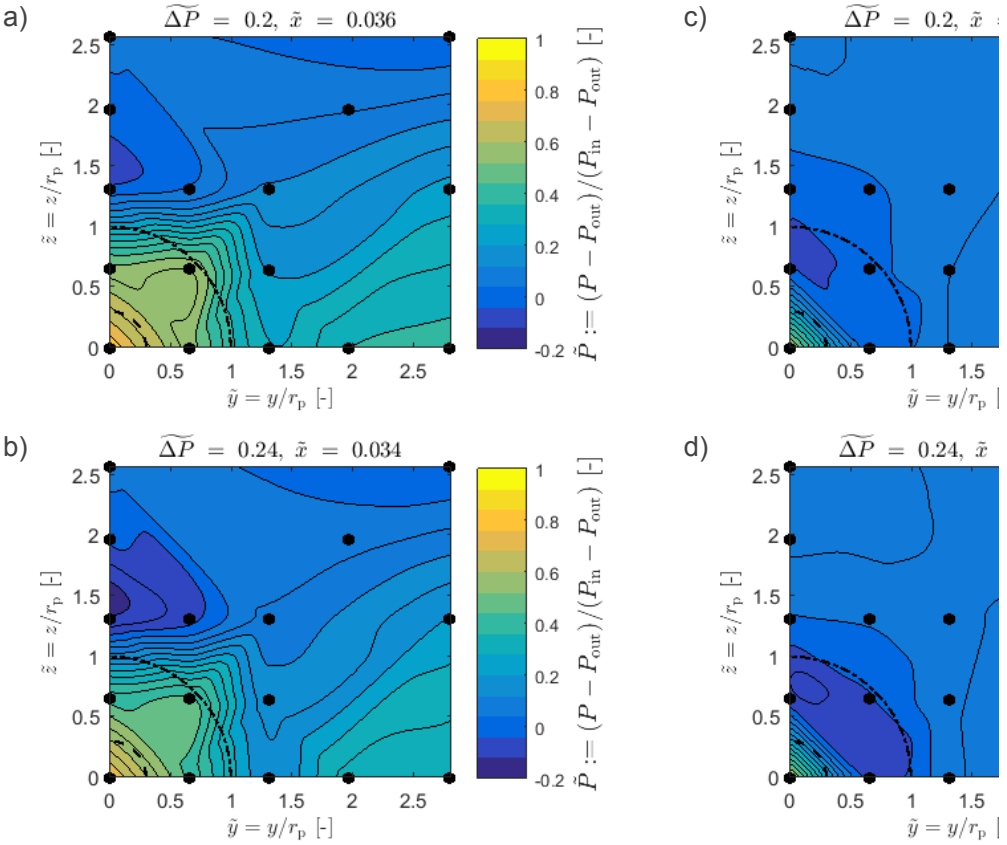

Figure 10. Pressure distribution on the bearing face for varying differential pressures and axial gap widths

Repeatabilty of force measurements. The friction force calibration was repeated multiple times within different days. Based on these tests, the repeatability of the load cell measurement could be assessed. The mean repeatability was determined to be in the range of ±(4 … 21) %. This uncertainty propagates to the uncertainty of F_{BF}, which is maximum 13.5 %.

3. TEST RESULTS

Fig. 10 compares 4 representative results of the reconstructed pressure field on the bearing face for various differential pressures $\widetilde{\Delta P} := (P_{in} - P_{out})/P_{in}$ and axial clearances $\tilde{x} := x_{BF}/r_p$. Herein, r_p is the radius of the feed pocket, which is embedded around the feed hole exit. A cubic spline interpolation was used to reconstruct the pressure measurement points.

The result basically corresponds to what has been expected and predicted by CFD. Near the feed hole region, the static pressures are maximum or rather close to P_{in} and decrease from there in z-direction towards the low pressure P_{out} at the top edge of the bearing face (~ radial flow regime). In y-direction the pressures first decrease and increase again while getting closer to the stagnation region (~ circumferential flow regime). A direct comparison between Fig. 10a) and c), respectively b) and d), shows, that the static pressure distribution changes with the axial gap width: The static pressures near the feed hole region are higher at small gap widths than at large gap widths. Furthermore, for small gap widths the expansion region around the feed hole is more extended and the overall pressure level is increased. What can also be observed is that the static pressure development qualitatively does not change significantly with the differential pressure, see Fig. 10a) and b), respectively c) and d). Quantitatively, the overall static pressure at the bearing face obviously increases with an increase of the differential pressure.

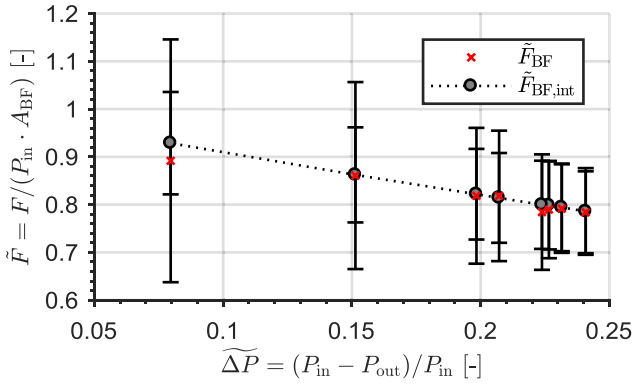

Figure 11. Comparison between $\tilde{F}_{BF}$ and $\tilde{F}_{BF,int}$

Based on the static pressure measurements the force acting on the bearing face can be determined. The reconstructed field of static pressures is integrated over the area of the bear-

ing face such that afterwards this integrated force $F_{\mathrm{BF,int}}$ can be compared to the force F_{BF} coming directly from the load cell. By doing so, the accuracy of the force measurements can be assessed. Fig. 11 represents the comparison between $\tilde{F}_{\mathrm{BF,int}} := F_{\mathrm{BF,int}}/(P_{\mathrm{in}} \cdot A_{\mathrm{BF}})$ and $\tilde{F}_{\mathrm{BF}} := F_{\mathrm{BF}}/(P_{\mathrm{in}} \cdot A_{\mathrm{BF}})$ for the case of ascending differential pressures and a non-varying axial gap width. The difference between both force results is maximum ±10 %. For descending differential pressures, the result looks alike and is therefore not shown here. The normalized force decreases with normalized differential pressure because the force increase is less than the increase of differential pressure. A linear relationship between the normalized force and the differential pressure is furthermore observable.

4. CONCLUSION

This paper presented a newly designed and built test rig for studying advanced sealing technology. The rig allows for a quick exchange of different seal / rotor designs and provides detailed pressure measurements on the bearing surface, accurate mass flow measurements and load cell measurements to investigate the seal / rotor force balance. Additionally, the rig allows for a very precise setting of the major seal operating parameters: the axial gap width can be adjusted during operation; for setting the radial gap width a quick disassembly is necessary; high differential pressure ratios, which are derived and scaled from real engine conditions, can be applied accurately.

The research on the rig results in high quality test data, which can be used to investigate the aerodynamic characteristics of advanced seals. A first focus was placed on the development of static pressures on the bearing surface. At increasing axial gap widths and non-varying differential pressures across the seal the pressure level on the bearing surface decreases. The expansion region furthermore weakens with increasing gap width. At increasing differential pressures and non-varying axial gap widths the pressure level increases quantitatively, but its distribution stays qualitatively alike. The static pressure results can additionally be used to determine the force acting on the bearing face so that the accuracy of the direct force measurement can be evaluated. Upcoming research on the rig will cover important quantities such as the stiffness or stability of the air bearing. The gained knowledge can subsequently be fed into rotating tests with a focus on a dynamic seal characterization and it can also be used to validate numerical models for the air bearing flow. This in the end allows for a goal-oriented optimization of new seal designs.

ACKNOWLEDGMENTS

This project has received funding from the European Union's Horizon 2020 research and innovation programme under grant agreement No. 653941. The authors would also like to thank various researchers at GE Global Research for useful discussions and inputs during the rig design.

NOMENCLATURE

A	[m^2]	Area.
F	[N]	Force.
$\dot{m}$	[kgs^{-1}]	Mass flow rate.
P	[bar]	Static pressure.
r	[m]	Radius.
u	[%]	Uncertainty.
x	[m]	Axial coordinate.

Subscripts and superscripts

BF	Bearing face.	LC	Load cell.
cav	Air cavity.	max	Maximum.
f	Friction.	out	Outlet.
id	Ideal.	p	Feed pocket.
in	Inlet.	∼	Dimensionless
int	Integration.		value.

REFERENCES

[1] Proposal of European Union's Horizon 2020 research and innovation programme FLEXTURBINE under grant agreement No. 653941. 2016.

[2] Hwang, M., Pope, A.N., 1996, "Advanced Seals for Engine Secondary Flowpath". *Journal of Propulsion and Power,* ***12****(4)*, pp. 794-799.

[3] Raparelli, T., Viktorov, V., Colombo, F., Lentini, L., 2016, "Aerostatic thrust bearings active compensation: Critical review". *Precision Engineering,* ***14***, pp. 1-12.

[4] Falaleev, S.V., Vinogradov, A.S., 2015, "Analysis of dynamic characteristics for face gas dynamic seals". *Procedia Engineering,* ***106***, pp. 210-217.

[5] Nishio, U., Somaya, K., Yoshimoto, S., 2011, "Numerical calculation and experimental verification of static and dynamic characteristics of aerostatic thrust bearings with small feed holes". *Tribology International,* ***44****(12)*, pp. 1790-1795.

[6] Fourka, M., Tian, Y., Bonis, M., 1996, "Prediction of the stability of air thrust bearings by numerical, analytical and experimental methods". *Wear,* ***198****(1-2)*, pp. 1-6.

[7] Franssen, R.H.M., Potze, W., de Jong, P., Fey, R.H.B., Nijmeijer, H., 2016, "Large amplitude dynamic behavior of thrust air bearings: modeling and experiments". *In press, accepted manuscript.*

[8] Yoshimoto, S., Yamamoto, M., Toda, K., 2006, "Numerical calculations of pressure distribution in the bearing clearance of circular aerostatic thrust bearings with a single air supply inlet". *Journal of Tribology,* ***129***, pp. 384-390.

[9] Gao, S., Cheng, K., Chen, S., Ding, H., Fu, H., 2015, "CFD based investigation on influence of orifice chamber shapes for the design of aerostatic thrust bearings at ultra-high speed spindles". *Tribology International,* ***92***, pp. 211-221.

[10] Zhou, Y., Chen, X., Chen, H., 2016, "A hybrid approach to the numerical solution of air flow field in aerostatic thrust bearings". *Tribology International,* ***102***, pp. 444-453.

[11] Blasiak, S., Zahorulko, A.V., 2016, "A parametric and dynamic analysis of non-contacting gas face seals with modified surfaces". *Tribology International,* ***94***, pp. 126-137.